Numerical Simulation of Fracture Failure Characteristics of Rock-Mass with Multiple Nonparallel Fractures Under Seepage Stress Coupling

Pengfei Wang · Yaoshe Xie

Abstract Based on the inclusion theory, the calculation formula of additional water pressure caused by the change of external stress state of fracture water in rock-mass is deduced, and its rationality and correctness are verified by numerical experiments. Then, using the rock fracture process analysis system RFPA2D-flow and considering the influence of additional water pressure, the fracture failure process of rock-mass with multiple (2, 3 and 4 fractures) nonparallel fractures (dip angles are not repeatedly selected from 0°, 30°, 45°, 60° and 90°) under the coupling action of stress and seepage is numerically simulated, and the following conclusions are obtained: (1) for rock-mass with two nonparallel fractures, large deformation and failure occur at the fracture position with an inclination of 0° because the fracture strike is perpendicular to the loading direction; In addition, the rock-mass first breaks at the fracture position with low strength, and gradually develops into overall failure, while the other fracture position is relatively complete. (2) For the rock-mass with 3 and 4 nonparallel fractures, similar to the rock-mass with 2 nonparallel fractures, the fracture failure of the rock-mass mainly occurs at the fracture position with low strength, the difference is that the number of fractures is more, and the rock bridge between fractures is connected, and the failure range is larger. (3) For the strength of fractured rock-mass, the fracture strength of rock-mass with multiple nonparallel fractures decreases gradually with the increase of fracture density.

Keywords Fluid solid coupling · Nonparallel fissure · Fracture failure characteristics · Numerical simulation

P. Wang · Y. Xie (✉)
State Key Laboratory of Coal Resources and Safe Mining, China University of Mining and Technology, Xuzhou 221116, China
e-mail: yaoshexcumt@126.com

P. Wang
School of Architecture and Civil Engineering, HuangShan University, Huangshan 245041, China

1 Introduction

The stress seepage coupling characteristics of fractured rock-mass have a significant impact on the stability of rock-mass engineering such as water conservancy, hydropower, energy and mining, and it is also one of the hot issues of rock mechanics in recent 20 years (Bisdom et al. 2017; Fekete and Diederichs 2013; Esaki et al. 1999; Olsson et al. 2001; Khang et al. 2004). The initiation, propagation and interconnection of fractures in rock-mass will lead to rock-mass deterioration and final fracture failure. This fracture failure behavior is more serious for fractured rock-mass under the combined action of in-situ stress and osmotic water pressure. Therefore, studying the fracture failure characteristics of fractured rock-mass

under hydraulic coupling has important theoretical and practical significance for the safety and stability of rock-mass engineering.

In recent years, many scholars have obtained rich theoretical results and field experience by means of theoretical analysis, physical experiments and numerical simulation. Kong et al. (2018) analyzed the lateral stress effect and seepage mechanism of single jointed rock-mass, and deduced the theoretical formula of seepage stress of single jointed rock-mass based on the permeability stress coupling analysis model of single jointed rock-mass. Sha and Zhang (2020) proposed a stress seepage damage coupling model to simulate the hydraulic splitting process of cylinder specimens with built-in cracks, the damage area obtained by numerical simulation is basically consistent with the range obtained by safety monitoring, which verifies the rationality of the proposed coupling model. Jia et al. (2019) used the particle flow program to study the crack propagation penetration mode and fracture mechanism of single fractured sandstone from the meso point of view, focusing on the effects of different medium principal stresses on the crack propagation and mechanical properties of single fractured sandstone. Rutqvist and Stephansson (2003) developed a multifunctional true triaxial fluid structure coupling test system to reveal the mechanical properties of coal and rock and the seepage law of fluid under the condition of true triaxial fluid structure coupling, the system can study the mechanical properties of coal and fluid seepage law under uniaxial, biaxial and true triaxial stress States under a variety of complex stress paths. Zhang et al. (2019) proposed the selection method of fluid solid coupling parameters of fractured coal and rock-mass in the numerical model based on the stress seepage experimental data of elastic coal samples and through fractured coal samples, combined with the cubic law of seepage, established the fluid solid coupling numerical model under triaxial loading, and simulated and analyzed the coupling characteristics of stress, fracture and seepage of coal samples during uniaxial and triaxial loading. Yin and Chen (2013) analyzed the variation trend of stress and displacement, joint hydraulic opening and transmittance with shear displacement through the pressure shear seepage test of 6 groups of artificial joint specimens with constant normal load and constant normal stiffness, and obtained the influence law of

seepage water pressure on the stress seepage coupling characteristics of jointed rock.

In previous studies, when analyzing the stress of fractured rock-mass, the fracture water in rock-mass is usually replaced by a fixed water pressure value, and then the fracture failure characteristics of fractured rock-mass are studied under certain boundary conditions (Man et al. 2015; Sheng et al. 2012; Li et al. 2010; Indraratna et al. 1998; Nuezil and Tracy 2010). The actual situation is that when the external stress state of fractured rock-mass changes, the shape of its internal fractures will change, resulting in additional water pressure due to the compression of fracture water, this additional water pressure is often the main reason for the fracture failure of fractured rock-mass. In addition, the fracture forms in rock-mass are different, and the complex fracture forms will also change the stress state of rock-mass and further affect the fracture failure characteristics of fractured rock-mass. Based on the existing research, the calculation formula of additional water pressure caused by the change of external stress state is derived, and its rationality and correctness are verified by numerical experiments; Then, using the rock fracture process analysis system RFPA2D-flow (Tsang and Witherspoon 1983; Amitrano 2006; Basarir 2006; Carpinteri et al. 2007) and considering the influence of additional water pressure, the fracture failure characteristics of rock-mass with multiple (2, 3 and 4 fractures) nonparallel fractures (dip angles of 0°, 30°, 45°, 60° and 90°) under the coupling action of stress seepage are numerically simulated.

2 Derivation of Calculation Formula of Additional Water Pressure in Fracture

For the common rock-mass with penetrating closed fractures in various rock-mass engineering, a plane model of single fracture rock-mass is established, as shown in Fig. 1. The included angle between the vertical principal axis of single fracture and rock-mass is α, the fractured rock-mass is in a saturated state, and the initial water pressure in the fracture is q_0. After being disturbed by engineering activities, the vertical and horizontal stresses are σ_1 and σ_3 respectively. It is assumed that the water pressure in the fracture changes to q_s.
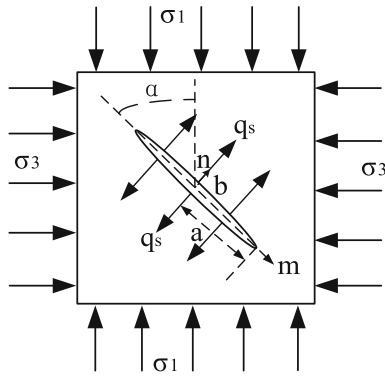
Fig. 1 Plane model of rock-mass with penetrating closed single fracture

For this plane strain problem, according to Eshelby's equivalent inclusion theory (Wang [2019]; Eshelby [1995]; Li et al. [2018]), assuming the fracture water as a linearly compressible homogeneous elastomer, the stress analysis of the fracture surface in the rock can be obtained:

$$\frac{\Delta\eta}{\eta_0} = -\frac{\Delta V_{cav}}{V_{cav}} = -\frac{\Delta S_{cav}}{S_{cav}} = k_w q_a \qquad (1)$$

where: $\Delta\eta$ is the change of liquid density; η_0 is the initial density of the liquid; ΔV_{cav} is the change of fracture volume; V_{cav} is the fracture volume; ΔS_{cav} is the change of fracture area; S_{cav} is the fracture area; k_w is the compressibility coefficient of fissure water in rock; q_a is the additional water pressure caused by the change of external stress state.

In addition, considering the flexibility tensor of dry fractures (Kachanov and Shafiro [1994]; Munjiza et al. [2013]), the relative area change $\Delta S_{cav}/S_{cav}$ of fractures can be expressed by the following equation:

$$\frac{S}{S_{cav}}\mathrm{tr}(H:\sigma) + q_a\left[\frac{S}{S_{cav}}\mathrm{tr}(H:I) - \frac{2(1+v)(1-2v)}{E}\right]$$
$$= -k_w q_a \qquad (2)$$

where: S is the area of the characterization unit; E and v are the elastic modulus and Poisson's ratio of linear elastic matrix respectively; σ is the external load tensor.

The fourth-order flexibility tensor H of fractures in rock-mass can be expressed as:

$$H = \frac{2(1-v^2)}{E}\frac{1}{S}\pi[a(2a+b)nnnn + (2b+a)mmmm$$
$$+ \frac{1}{2}(a+b)^2(mn+nm)^2 - ab(mmnn+nnmm)] \qquad (3)$$

where: a is the length of the long axis of the elliptical fracture; b is the length of the minor axis of the elliptical fracture; m is the direction vector of the long axis a of the elliptical fracture; n is the direction vector of the minor axis b of the elliptical fracture.

For elliptical fractures, $\xi = b/a \ll 1$, substitute Eqs. (3) into (2), and the additional water pressure caused by the change of external stress state can be obtained as:

$$q_a = -\frac{1}{1+\delta}\sigma_d \qquad (4)$$

$$\delta = \xi\frac{k_w E - 2(1+v)(1-2v)}{2(1-v^2)} \qquad (5)$$

where: ξ is the shape parameter of elliptical fracture; σ_d is the force generated by the external load in the normal direction of the fracture surface, which can be expressed as:

$$\sigma_d = -\left(\frac{\sigma_1+\sigma_3}{2} - \frac{\sigma_1-\sigma_3}{2}\cos 2\alpha\right).$$

Substitute σ_d into Eq. (4) to obtain:

$$q_a = \frac{\phi}{1+\delta}\left(\frac{\sigma_1+\sigma_3}{2} - \frac{\sigma_1-\sigma_3}{2}\cos 2\alpha\right) \qquad (6)$$

Under the action of external load, fracture water will flow into the rock, resulting in the decrease of additional water pressure. Therefore, a reduction coefficient ϕ is introduced into Eq. (6) to describe this phenomenon, and $0 < \phi < 1$.

To sum up, the total water pressure generated by fissure water in rock-mass under external load is:

$$q_s = q_0 + q_a$$
$$= q_0 + \frac{\phi}{1+\delta}\left(\frac{\sigma_1+\sigma_3}{2} - \frac{\sigma_1-\sigma_3}{2}\cos 2\alpha\right) \qquad (7)$$

3 Verification of Theoretical Derivation Results

In order to verify the correctness and rationality of the theoretical derivation results, this section uses the rock

fracture process analysis system RFPA[2D]-flow to carry out numerical simulation research on the fracture failure process of prefabricated single fractured rock-mass with different dip angles (0°, 30°, 45°, 60° and 90°) under the coupling action of stress and seepage under the consideration of additional water pressure, the calculated values of additional water pressure are compared with the numerical simulation results.

RFPA[2D]-flow software is a stress-seepage-damage coupling analysis system (Ma et al. 2020; Man et al. 2015), its calculation method is based on finite element and statistical damage theory, considers the non-uniformity of material properties and the randomness of defect distribution, and adopts the following basic assumptions: (1) the fluid in rock material medium follows Biot consolidation theory; (2) The rock medium is an elastic brittle material with residual strength, and its mechanical behavior during loading and unloading conforms to the elastic damage theory; (3) The maximum tensile strength criterion and Mohr Coulomb criterion are used as the damage threshold to judge the damage of the element; (4) In the elastic state, the relationship between stress and seepage coefficient is described by negative exponential equation; (5) The mechanical parameters (elastic modulus, strength and Poisson's ratio) of the material mesostructure are assigned according to the Weibull distribution.

The material mechanical parameters of the numerical model of fractured rock-mass are shown in Table 1.

The size of numerical model of fractured rock-mass is φ 50 mm × 100 mm, fracture length 18 mm, width 0.3 mm. In order to consider the influence of additional water pressure, the water body in the fracture is simplified as an elastomer, and the initial water pressure is applied on the fracture surface. The numerical model of prefabricated single fracture rock-mass with different dip angles is shown in Fig. 2. During the simulation calculation, the
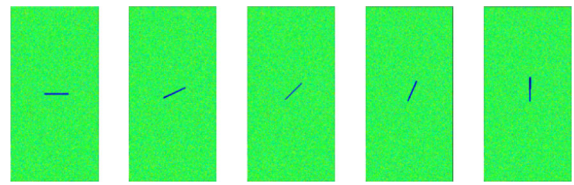

Fig. 2 Numerical model of prefabricated single fracture rock-mass with different dip angles

confining pressure of 8.0 MPa and the initial water pressure in the fracture are applied to the model. The loading method adopts the displacement negative increment loading in the y-axis direction, and the single step increment of positioning displacement is set as 1×10^{-4} m/step, the preset number of loading steps is 100, and the step-by-step calculation is carried out automatically.

Table 2 shows the comparison between the theoretical calculation value of additional water pressure in prefabricated single fractured rock with different dip angles and the numerical simulation results when the confining pressure is 8.0 MPa and the initial water pressure is 3.0 MPa, it can be seen that the overall difference is small, which also proves the correctness of the calculation formula of additional water pressure in fractured rock deduced in Sect. 2. When the fracture dip angle is 45°, the error between the theoretical calculation results and the numerical simulation results is large. The reason is that the water body is different from the elastomer, in order to facilitate the analysis, the water body is taken as the elastomer for approximate calculation. It should be noted that the additional water pressure values in Table 2 are obtained when the fractured rock-mass reaches its fracture strength (initial fracture failure occurs along the rock itself or fracture).

Figure 3 selects four landmark stages in the loading process, step 1–6, step 35–17, step 36–4 and step 36–6, showing the fluid solid coupling RFPA numerical simulation fracture failure process of prefabricated

Table 1 Mechanical parameters of model materials

Density (g cm^{-3})	Elastic modulus (GPa)	Poisson's ratio	Compressive strength (MPa)	Tensile strength (MPa)	Cohesion (MPa)	Residual strength coefficient	Initial permeability coefficient (m/d)	Initial water pressure (MPa)
2.207	13.19	0.12	49.2	3.36	13.93	0.1	0.1	0.6

Table 2 Comparison between theoretical calculation and numerical simulation results of additional water pressure

Fracture dip angle (°)	q_a(MPa)		Error (%)
	Theoretical calculation results	Numerical simulation results	
0	2.012	2.027	0.745
30	5.983	6.013	0.501
45	10.578	11.013	4.112
60	14.109	13.988	0.857
90	18.368	18.284	0.457

(a) Spatiotemporal evolution of macroscopic failure

(b) Temporal and spatial evolution of acoustic emission activities

(c) Spatiotemporal evolution of displacement vector
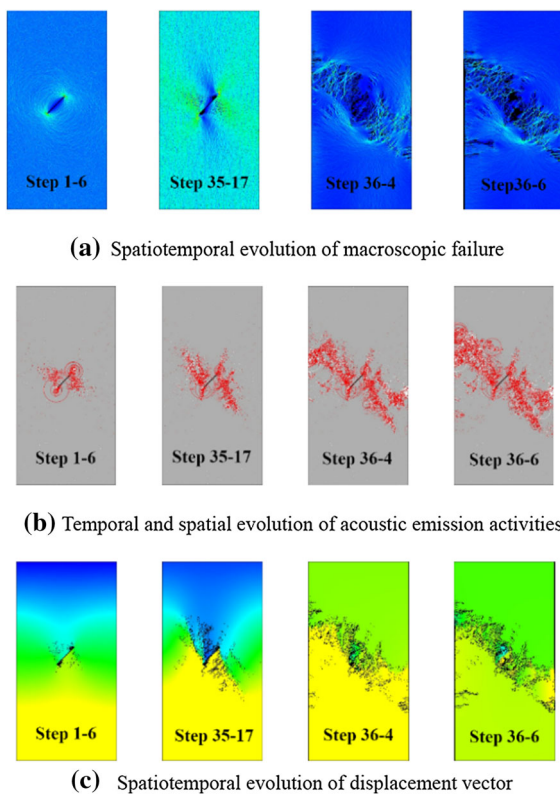
Fig. 3 Fluid solid coupling RFPA numerical simulation of fracture failure process of prefabricated single fracture rock with 45° inclination

single fracture rock with 45° inclination. Among them, Fig. 3a shows the macro failure results of four landmark stages respectively, the black area in the picture represents the distribution range of plastic area in the sample, and other colors represent the difference of principal stress at each position in the sample; Fig. 3b shows the acoustic emission results of four landmark stages respectively. The acoustic emission is represented by a red circle, the dot represents the position where the acoustic emission occurs, and the diameter of the circle represents the size of the acoustic emission energy; Fig. 3c shows the distribution of plastic zone in rock samples at four landmark stages and the difference of vertical deformation at each position.

According to the comprehensive analysis of Fig. 3a, b, when the simulation calculation reaches the loading steps 1–6, the model basically maintains linear elasticity, under the influence of water pressure, micro fractures appear at both ends of the prefabricated fractures in the model, and acoustic emission activities also appear slightly in this area; From the simulation calculation to the 36–4 loading step, the fracture failure activities in the model are still mainly concentrated near the prefabricated fractures, the wing cracks expand rapidly, and the acoustic emission activities converge and surge; When the simulation calculation reaches the loading step 36–6, the model has broken along the internal prefabricated fractures, and then the failure activities will continue to expand to other areas inside the model, resulting in the shear or splitting failure of the whole model.

Figure 3c shows the temporal and spatial evolution process of displacement vector (Y direction) in the simulation calculation of prefabricated single fracture rock-mass with 45° inclination. It can be seen that from the 1–6 loading step to the 36–4 loading step, the change of displacement vector is greatly affected by the fracture failure activity of prefabricated fractures in the model, which is basically consistent with the propagation direction of prefabricated fractures; During the simulation calculation to the 36–6 loading step, the displacement vector has little difference as a whole because the model has broken along the internal prefabricated fracture.
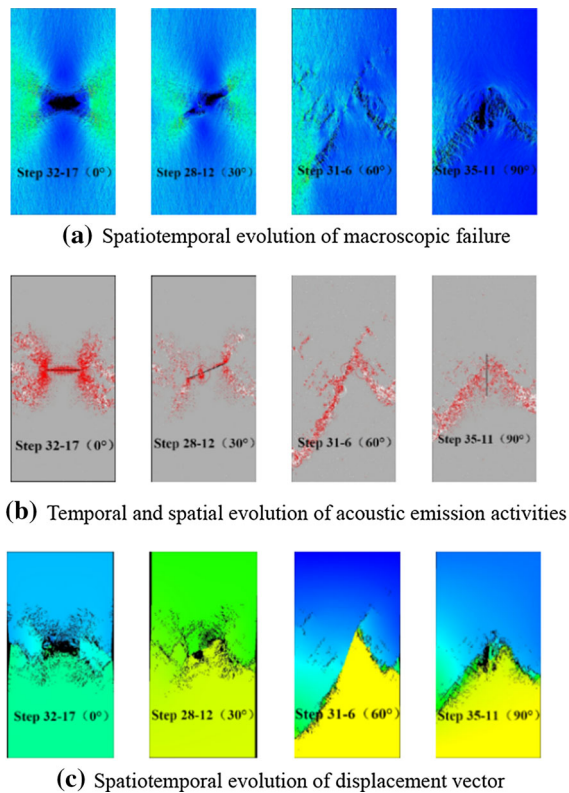
(a) Spatiotemporal evolution of macroscopic failure

(b) Temporal and spatial evolution of acoustic emission activities

(c) Spatiotemporal evolution of displacement vector

Fig. 4 Final results of fluid structure coupling RFPA numerical simulation of prefabricated single fracture rock with dip angles of 0°, 30°, 60° and 90°

Figure 4a, b show the final results of fracture failure and acoustic emission activity evolution of prefabricated single fracture rock-mass with dip angles of 0°, 30°, 60° and 90°. The comprehensive analysis shows that under the coupling action of stress and seepage, shear and tension failure finally occur in the rock-mass with prefabricated fractures with different dip angles. The acoustic emission activity intensity near the prefabricated fractures is significantly higher than that in other locations, but the wing crack propagation direction is different due to the different dip angles of the prefabricated fractures; Fig. 4c shows the final results of displacement vector evolution (Y direction) of numerical simulation test of precast fractured rock-mass with dip angles of 0°, 30°, 60° and 90°. It can be seen that the variation of internal displacement vector of rock-mass with prefabricated fractures with different dip angles is consistent with the fracture propagation direction, and the deformation of the upper part of the rock is obviously greater than that of the lower part.

4 Numerical Simulation Test Scheme of Rock-Mass with Multiple Nonparallel Fractures

4.1 Numerical Simulation Test Scheme

This section continues to use the rock fracture process analysis system RFPA2D-flow and consider the influence of additional water pressure to conduct numerical simulation research on the fracture failure characteristics of rock-mass with multiple (2, 3 and 4 fractures) nonparallel fractures (dip angles are not repeatedly selected from 0°, 30°, 45°, 60° and 90°) under the coupling action of stress seepage, the model size is φ 50 mm × 100 mm, row and column grid is divided into 800 × 400, fracture length 18 mm, width 0.3 mm. For the fracture spacing, the distance between the top fracture center point and the upper surface of the rock sample and the bottom fracture center point and the lower surface of the rock sample is 20 mm. In addition, if there are 2 nonparallel fractures, the distance between the center points of the two fractures is 60 mm; When there are 3 nonparallel fractures, the distance between the center points of the two fractures is 30 mm; When there are 4 fractures, the distance between the center points of the two fractures is 20 mm, as shown in Fig. 5.

The material mechanical parameters of the numerical model of fractured rock-mass are the same as those in the previous section, the numerical model of rock-mass with multiple nonparallel fractures is shown in Fig. 6.

During the simulation calculation, the confining pressure of 8.0 MPa is applied to the model, and the water pressure applied in the fracture includes two parts: initial water pressure and additional water pressure. The initial water pressure is 3.0 MPa. For
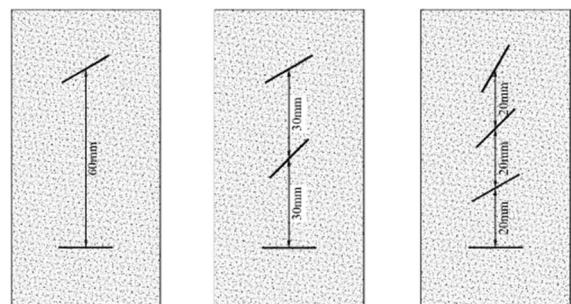

Fig. 5 Schematic diagram of fracture spacing of rock mass with multiple nonparallel fractures

(a) Two nonparallel fractures

(b) Three nonparallel fractures

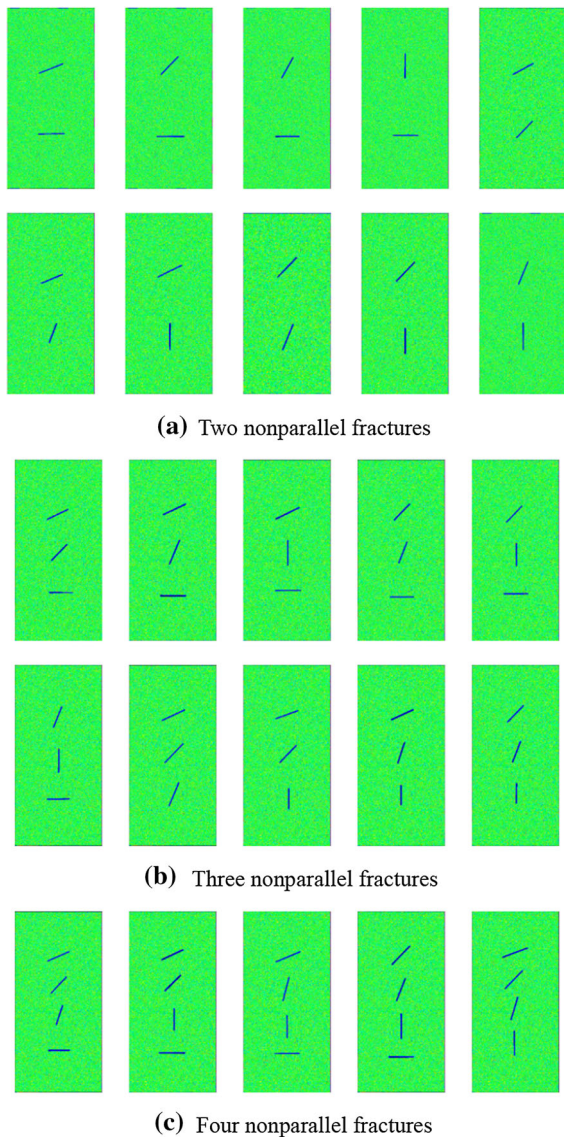**(c)** Four nonparallel fractures

Fig. 6 Numerical model of rock-mass with multiple nonparallel fractures

the additional water pressure, as in Sect. 3 of this paper, the water body is simplified as an elastomer, and the value of the additional water pressure is obtained through numerical simulation test. In addition, the loading mode adopts the negative displacement increment loading in the y-axis direction, and the single step increment of positioning displacement is set as 1×10^{-4} m/step, the preset number of loading steps is 100, and the step-by-step calculation is carried out automatically.

4.2 Analysis of Numerical Simulation Test Results

Figure 7 shows the macro failure results, acoustic emission activity results and deformation vector results of rock-mass with two nonparallel fractures.
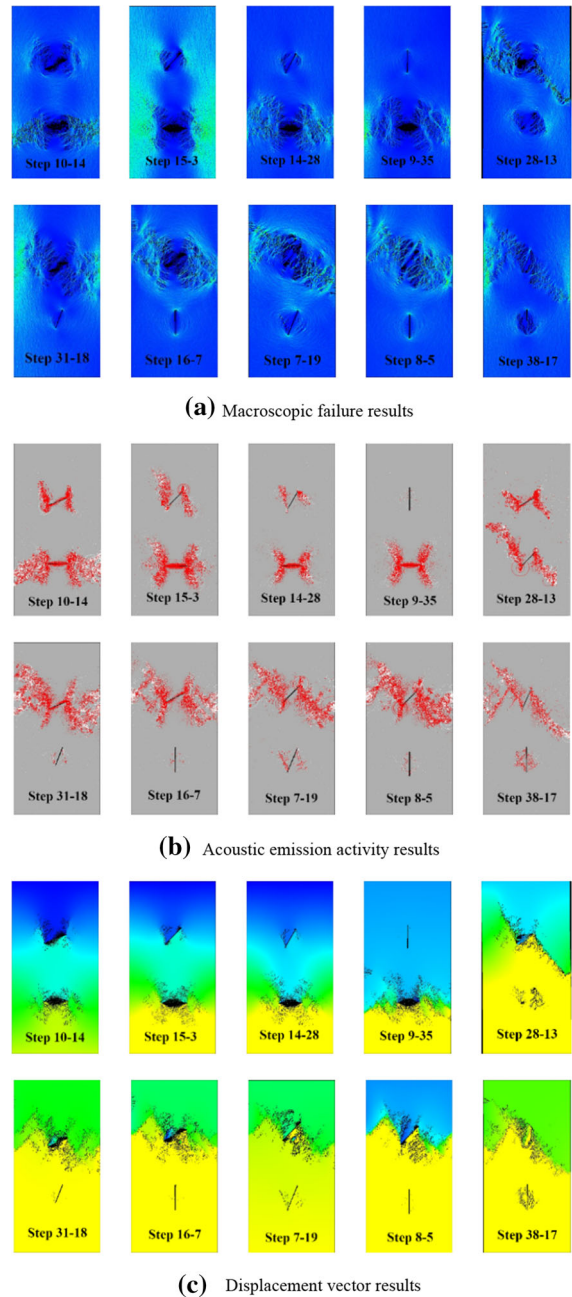

(a) Macroscopic failure results

(b) Acoustic emission activity results

(c) Displacement vector results

Fig. 7 Numerical simulation test results of fluid solid coupling RFPA in rock-mass with two nonparallel fractures

It can be seen that for the rock-mass with two fractures with dip angles of (0°, 30°), (0°, 45°) and (0°, 60°), the y-direction deformation of the specimen during loading is large because the (horizontal) trend of the 0° dip fracture is perpendicular to the test loading direction, in addition to shear failure along the 30°, 45° and 60° dip fractures, large deformation and failure also occurred at the fracture position with an inclination of 0°; In addition, compared with 30° and 60° dip fractures, the damage of 45° dip fractures is significantly more serious, and the damage of 60° dip fractures is the weakest, indicating that the strength of fractures is the lowest when the dip angle is 45°. For the rock-mass with two fractures with dip angles of (0°, 90°), (30°, 90°), (45°, 90°) and (60°, 90°), since the strike of the 90° fracture (vertical) is parallel to the test loading direction, it has little influence on the deformation and strength of the fractured rock-mass during loading, therefore, the fractured rock-mass only occurs shear failure along the dip angles of 0°, 30°, 45° and 60°. When the dip angles of two fractures in the rock are (30°, 45°), (30°, 60°) and (45°, 60°), the rock-mass first breaks at the fracture position with low strength, and gradually develops into overall failure, while the position of the other fracture is relatively complete.

It should be pointed out that for the same rock-mass, due to the different inclination angles of each fracture in the rock-mass, the additional water pressure generated in each fracture of the rock-mass is also different with the application of external load. Therefore, in the numerical simulation calculation of rock-mass with two nonparallel fractures, taking the stress condition of the first fracture failure of fractured rock-mass (along the fracture or rock-mass with the weakest strength) as the standard, the additional water pressure value is given to the two fractures in the rock body respectively, which is the same for rock-mass with three nonparallel fractures and rock-mass with four nonparallel fractures, no more details.

Figure 8 shows the macro failure results, acoustic emission activity results and deformation vector results of rock-mass with three nonparallel fractures. It can be seen that the rock-mass with three fractures with dip angles of (0°, 30°, 45°), (0°, 30°, 60°), (0°, 30°, 90°, (0°, 45°, 60°), (0°, 45°, 90°) and (0°, 60°, 90°) is the same as the rock-mass with two nonparallel fractures, the rock-mass first breaks at the horizontal fractures and fractures with low strength, then it
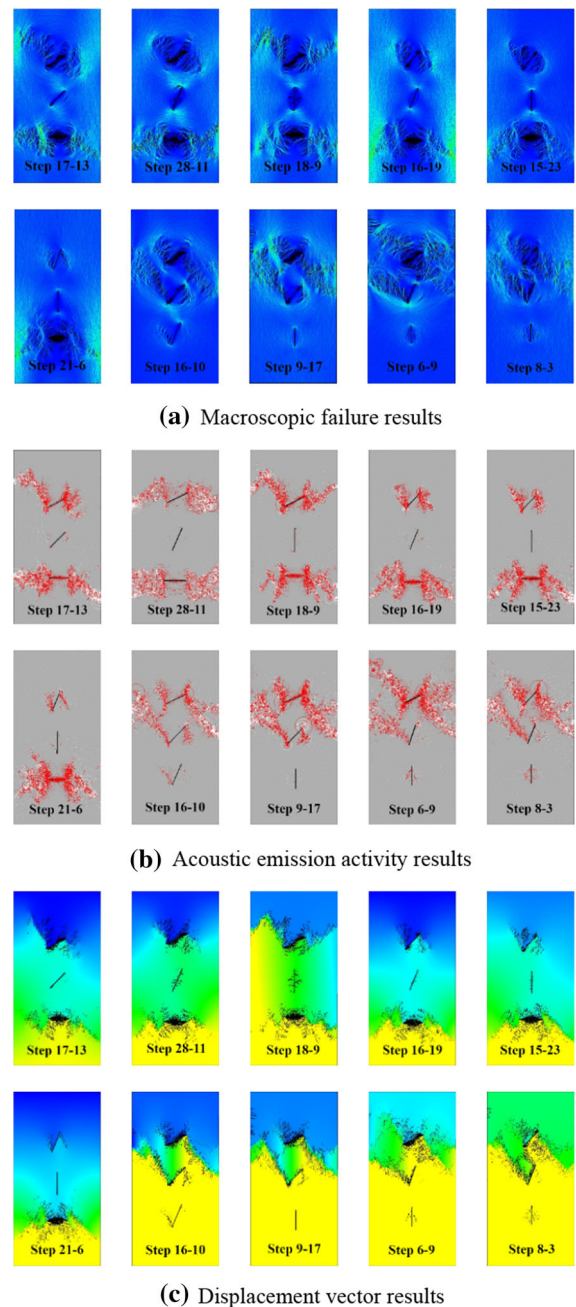

(a) Macroscopic failure results

(b) Acoustic emission activity results

(c) Displacement vector results

Fig. 8 Numerical simulation test results of fluid solid coupling RFPA in rock-mass with three nonparallel fractures

extends to the periphery, but it is relatively complete at the middle fracture, the cloud map of displacement vector results can also be divided into three parts with the upper and lower fractures as the boundary; For the rock-mass with three fractures with dip angles of (30°, 45°, 60°), (30°, 45°, 90°), (30°, 60°, 90°) and (45°, 60°,

90°), the deformation and failure of the rock-mass at the vertical fracture position are relatively weak, however, due to the increase of fracture density, the rock bridge between the fractures is broken during loading, resulting in the rapid decline of rock-mass strength.

Figure 9 shows the macro failure results, acoustic emission activity results and deformation vector results of rock-mass with four nonparallel fractures. It can be seen that, like the rock-mass with three nonparallel fractures, the rock-mass with four nonparallel fractures also has fracture failure at the horizontal fractures and fractures with low strength, but the failure range has not been significantly expanded.

Figure 10 shows the stress–strain curves of rock-mass with two fractures (30°, 45°), three fractures (30°, 45°, 60°) and four fractures (0°, 30°, 45°, 60°) during the numerical simulation test. It can be seen that when the peak strength is reached, the y-direction deformation of rock-mass with two nonparallel fractures, three nonparallel fractures and four nonparallel fractures is almost the same, because for rock-mass with multiple nonparallel fractures, the internal failure area is mainly concentrated at the horizontal fractures
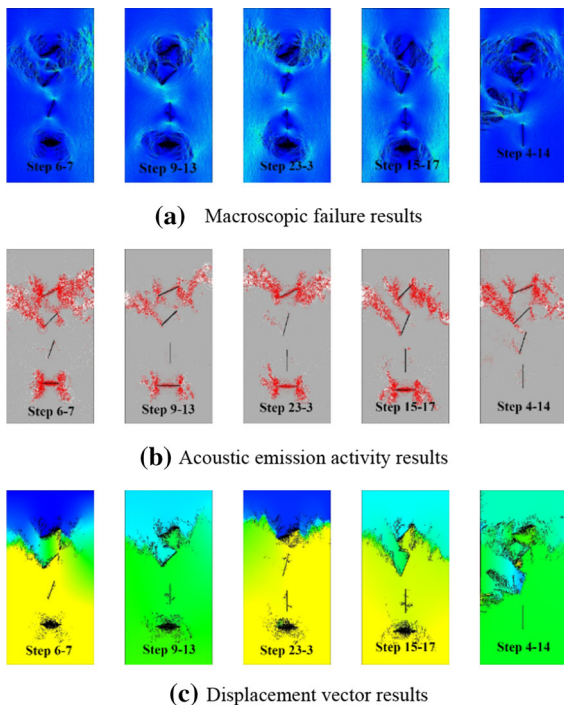
(a) Macroscopic failure results

(b) Acoustic emission activity results

(c) Displacement vector results

Fig. 9 Numerical simulation test results of fluid solid coupling RFPA in rock-mass with four non parallel fractures

(a) Fracture dip angle (30 °, 45 °)

(b) Fracture dip angle（30°，45°，60°）
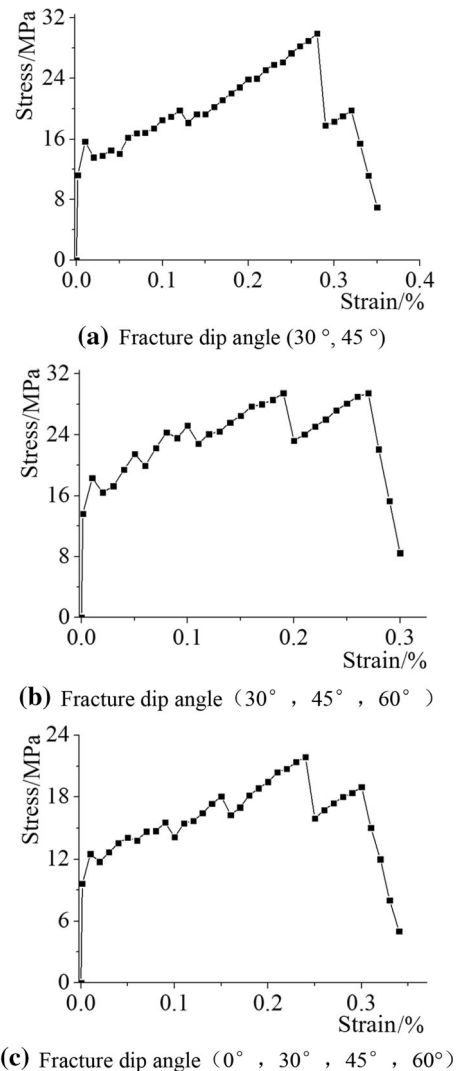
(c) Fracture dip angle（0°，30°，45°，60°）

Fig. 10 Stress–strain curve of rock-mass with multiple nonparallel fractures

and fractures with low strength during loading, and finally forms an overall failure, it does not develop to the fracture position with high strength; As for the peak strength, the peak strength of rock-mass with two fractures (30°, 45°) is 31.5 MPa, the peak strength of rock-mass with three fractures (30°, 45°, 60°) is 29.7 MPa, and the peak strength of rock-mass with four fractures (0°, 30° 45°, 60°) is 21.3 MPa, indicating that with the increase of the number of fractures, the strength of rock-mass with multiple nonparallel fractures also decreases gradually.

5 Conclusions

Based on the inclusion theory, the calculation formula of additional water pressure caused by the change of external stress state of fracture water in rock-mass is deduced, and its rationality and correctness are verified by numerical experiments. Then, using the rock fracture process analysis system RFPA2D-flow and considering the influence of additional water pressure, the fracture failure characteristics of rock-mass with multiple (2, 3 and 4 fractures) nonparallel fractures (dip angles are not repeatedly selected from 0°, 30°, 45°, 60° and 90°) under the coupling action of stress and seepage are numerically simulated, and the following conclusions are obtained:

1. For rock-mass with two nonparallel fractures, large deformation and failure occur at the fracture position with an inclination of 0° because the fracture strike is perpendicular to the loading direction; In addition, the rock-mass first breaks at the fracture position with low strength, and gradually develops into overall failure, while the other fracture position is relatively complete.

2. For the rock-mass with 3 and 4 nonparallel fractures, similar to the rock-mass with 2 nonparallel fractures, the fracture failure of the rock-mass mainly occurs at the fracture position with low strength, the difference is that the number of fractures is more, and the rock bridge between fractures is connected, and the failure range is also larger.

3. For the strength of fractured rock-mass, the fracture strength of rock-mass with multiple nonparallel fractures decreases gradually with the increase of fracture density.

Author Contributions All the authors contributed extensively to the work. PW carried out numerical simulation research and wrote the paper. YX draw the figure and collected data of numerical simulation.

Declarations

Conflict of interest The authors declare that they have no conflict of interest to declare.

References

Amitrano D (2006) Rupture by damage accumulation in rocks. Int J Fract 139(3):369–381

Basarir H (2006) Engineering geological studies and tunnel support design at Sulakyurt dam site. Turk Eng Geol 86(4):225–237

Bisdom K, Nick HM, Bertotti G (2017) An integrated workflow for stress and flow modelling using outcrop-derived discrete fracture networks. Comput Geosci 103:21–35

Carpinteri A, Lacidogna G, Pugno N (2007) Structural damage diagnosis and life-time assessment by acoustic emission monitoring. Eng Fract Mech 74(1):273–289

Esaki T, Du S, Mitaniy Y et al (1999) Development of a shear-flow test apparatus and determination of coupled properties for a single rock joint. Int J Rock Mech Min Sci 36(5):641–650

Eshelby JD (1995) The determination of the elastic field of an ellipsoidal inclusion and related problems. Math Phys Eng Sci 10:376–396

Fekete S, Diederichs M (2013) Integration of three-dimensional laser scanning with discontinuum modelling for stability analysis of tunnel in blocky rockmasses. Int J Rock Mech Min Sci 57:11–23

Indraratna B, Haque A, Aziz N (1998) Laboratory modelling of shear behavior of soft joints under constant normal stiffness conditions. Geotech Geol Eng 16(1):17–44

Jia P, Zhang Y, Liu DQ et al (2019) Particle flow simulation of failure process in single fissured sandstone under true triaxial compression. J Northeastern Univ 40(11):1654–1659

Kachanov T, Shafiro B (1994) Effective moduli of solids with cavities of various shapes. Appl Mech Rev 47(1):151–174

Khang ND, Watanabe K, Sawgusa H (2004) Fracture step structure: geometrical characterization and effects on fluid flow and breakthrough curve. Eng Geol 75:107–127

Kong Y, Zhu ZD, Ruan HN (2018) Stress-seepage coupling characteristics of jointed rock mass under three principal stresses. Rock Soil Mech 39(6):2008–2015

Li G, Tang CN, Li LC et al (2010) Numerical simulation of 3D hydraulic fracturing process. Chin J Geotech Eng 32(12):1875–1881

Li DQ, Li ZL, Lv CC (2018) Analysis of fracture strength of rock mass considering fissure additional water pressure. Rock and Soil Mechanics 39(9):3173–3180

Man K, Liu XL, Su R et al (2015) Permeability measuring of large scaled single fractured media with a seepage-stress coupling testing apparatus. Chin J Rock Mech Eng 34(10):2064–2072

Munjiza A, Owen DRJ, Bicanic N (2013) A combined finite-discrete element method in transient dynamics of fracturing solids. Eng Comput 12(2):145–174

Neuzil CE, Tracy JV (2010) Flow through fractures. Water Resour Res 17(1):191–199

Olsson R, Barton N (2001) An improved model for hydromechanical coupling during shearing of rock joint. Int J Rock Mech Min Sci 38(3):317–329

Rutqvist J, Stephansson O (2003) The role of hydromechanical coupling in fractured rock engineering. Hydrogeol J 11(1):7–40

Sha S, Zhang GX (2020) Simulation of 3D hydraulic fracturing of concrete gravity dams based on stress-seepagedamage coupling model. J China Inst Water Resour Hydropower Res 18(1):1–11

Sheng JC, Li FB, Yao DS et al (2012) Experimental study of seepage properties in rocks fracture under coupled hydro mechano chemical process. Rock Soil Mech 31(5):1016–1025

Tsang YW, Witherspoon PA (1983) The dependence of fracture mechanical and fluid flow properties on fracture roughness and sample size. J Geophys Res Solid Earth 88(B3):2359–2366

Wang PF (2019) (2019) Study on evolution mechanism of fracture and seepage of fault zone rockmass under osmotic pressure. University of Science and Technology Beijing, Beijing

Yin LM, Chen JT (2013) Experimental study of influence of seepage pressure on joint stress-seepage coupling characteristics. Rock Soil Mech 34(9):2563–2568

Zhang C, Tu SH, Zhao YX et al (2019) Discrete element numerical simulation of triaxial fluid solid coupling based on seepage experiment. J Min Sci Technol 4(1):23–33